PIV investigation of two-phase flow in a micro-pillar microfluidic device

Gianluca Blois^{1,2,3}, Julio M. Barros¹ and Kenneth T. Christensen^{1,2,3}

¹ Department of Mechanical Science and Engineering, University of Illinois, Urbana-Champaign, USA blois@illinois.edu, jmbarros@illinois.edu, ktc@illinois.edu

² Department of Geology, University of Illinois, Urbana-Champaign, USA

ABSTRACT

Here we report on the dynamics of immiscible fluid displacement in porous media at the microscale captured with microscopic particle image velocimetry (μ PIV). The experimental challenges associated with simultaneously imaging two immiscible fluids, tracking their interface and quantifying the flow processes induced by the fluid-fluid interaction are discussed and an imaging method coupling refractive index matching and fluorescent signal separation is described. The technique was first applied to single-phase flow for validation and then to two-phase flows in porous micromodels. Both drainage and imbibition in a regular pore network were considered herein with a focus on interface migration and effects owing to the passage of the interface. The velocity distribution obtained for these experimental conditions revealed several flow peculiarities. In particular, the instabilities associated with the interfacial processes propagate downstream and perturb the flow field, resulting in dramatic differences from the regular flow paths typical of steady-state, single-phase flow. Additionally, the passage of the interface does not restore previous flow patherns but instead yields complex preferential flow paths that mutually interact with residual trapped pockets of fluid.

INTRODUCTION

Understanding the dynamics of immiscible multiphase fluid flows in porous media is relevant to a multitude of fields in science and engineering. Applications include, among others, mass transfer in porous catalysis, mobilization of trapped hydrocarbon in enhanced oil recovery and, more recently, membrane-based fuel cells and geological carbon sequestration. In such applications, processes are driven by the injection/suction of a certain fluid phase into/from a porous domain saturated with another fluid, resulting in a moving fluid-fluid interface (i.e., *front*). For example, due to its low viscosity, supercritical CO₂ can be easily injected into natural hydrocarbon geophysical reservoirs through which it migrates, displacing the previous saturating fluid (e.g. natural gas, brine).

Due to difficulties associated with achieving direct measurements in a solid porous matrix with a complex geometry, these multiphase systems are typically numerically modeled. The most common numerical models to predict flow and transport in porous media over smaller length scales include Lattice-Boltzmann (LB), smoothed particle hydrodynamics (SPH) and direct numerical simulation (DNS) techniques. Larger-scale studies rely on volume-averaged methods that provide macro-scale (several km) predictions of CO₂ migration through reservoirs (MacMinn et al., 2010). A recent review of these methods can be found in Meakin and Tartakovsky (2009). However, the physical processes occurring at the pore scale and the dynamics of the fluid-fluid interface are poorly understood, thus hampering the development of robust numerical models and limiting their predictive ability. The main reason for this roadblock is due to a lack of experimental data at these small scales in representative porous environments.

A peculiarity of multiphase flows in porous media is that mutual fluid-fluid and fluid-solid interactions occur. While macroscopic flow of a homogeneous fluid through low-permeability media is mainly governed by viscous forces (fluid-solid interaction only) and can thus be faithfully predicted by Darcy's law, multiphase flow dynamics result from the competition between, viscous, capillary and driving forces (e.g. gravitational force, pressure gradient). The competition between viscosity and surface tension may result in meniscus instabilities. These instabilities govern the morphology and displacement of the fluid-fluid front giving rise to a number of non-linear processes. Some of these lead to the onset of turbulence, while others involve bubble formation. In all these cases, flow becomes irreversible and the onset of hysteretic behavior occurs (Jerauld and Salter 1990).

Due to the complexity of the physics of multiphase flow in porous media, experimental methods remain the most reliable tool to achieve a better understanding of these systems. Many of these methods are based upon visualization of the flow permeating through a 2D (two-dimensional) porous matrix with the goal of characterizing the interface migration and the degree of fluid saturation. Fundamental flow processes at the pore scale were first investigated by Lenormand et al. (1983) in simple micromodels using qualitative approaches. These studies led to the definition of

³ International Institute for Carbon Neutral Energy Research (WPI-I2CNER), Kyushu University, 744 Moto-oka, Nishi-ku, Fukuoka 819-0395, Japan

basic mechanisms of microscale multiphase flow (e.g. piston-type motion, snap-off). These notions were then used as a basis for the study of larger porous networks. Lenormand et al. (1988) used a wide range of viscosity ratios, $M = \mu_d/\mu_r$ (where, μ_d and μ_r are displacing and resident fluid, respectively) and Capillary numbers, $Ca = v \mu_d/\sigma$ (where v is the average pore scale velocity of the displacing fluid and σ is the interfacial tension) for a range of porous structures, interacting fluids and boundary conditions. They identified several flow regimes (i.e. stable displacement, capillary and viscous fingering) and proposed a phase diagram linking dominating forces to front morphology and trapping mechanisms.

As pointed out for the first time by Haines (1930) and confirmed by several recent observations (Berg et al., 2013), the motion of a fluid front is extremely unsteady and characterized by pore-scale jumps, known as *Haines jumps* or *Rheon*. These phenomena consist of energetic pore-scale bursts that displace the fluid from a pore throat into a wider pore space and are associated with a sudden drop in capillary pressure. Understanding Haines jump dynamics is extremely important for developing accurate conceptual and numerical models of two-phase flow that can predict critical pore-space processes. Haines jumps are in fact associated with mechanisms of accumulation of resident fluid within intergranular interstices (i.e., trapping) and provide information on structure and distribution of such residual ganglia. The identification of these phenomena have mainly relied upon high-resolution monitoring of capillary pressure (Crawford et al., 1966; Yuan and Swanson, 1989; Moebius and Or, 2012). Use of simple (single-layer) porous media allowed Moebius and Or (2012) to demonstrate the strong correlation between time history of pressure bursts and interfacial pore-scale jumps. Experimental studies quantified the speed of these pore-scale events, highlighting that pore-space fluid can achieve velocities that may be three orders of magnitude higher than mean flow, resulting in Reynolds numbers, *Re*, in the turbulent regime. As a consequence, despite the small length scales involved, inertial forces may play a critical role in front migration.

Despite the importance of these phenomena, energy dissipation mechanisms and phase entrapment processes remain poorly understood. Moreover, the linkage between pore-scale flow processes and fluid-front dynamics remain largely unquantified. In fact, while several attempts have been made to develop a qualitative description of fluid interactions between neighboring pores along displacement fronts in 2D (Zhang et al., 2011) and in 3D (Berg et al., 2013; Krummel et al., 2013) porous structures, experimental studies reporting quantification of multiphase flow velocity in pore spaces are not available. To this end, we use microfluidic devices and a dual-camera µPIV setup to quantitatively observe the dynamic interaction between two immiscible fluids within a regular 2D permeable domain. The main objectives of this paper are to present the technique and to report results from preliminary experiments.

EXPERIMENTAL SETUP

Experiments were conducted using micromodels in which a 2D regular permeable network was etched (Fig. 1). The microchannels were fabricated in PDMS (Polydimethylsiloxane) using a standard soft lithography technique wherein the master was manufactured using photolithography. The microchannel consisted of an inlet channel, a 2D permeable channel (20 mm long, 10 mm wide and $h = 25 \,\mu\text{m}$ deep) in which measurements were made, and an outlet channel. The solid matrix of the permeable channel consisted of uniform size cylindrical pillars (diameter $D = 300 \,\mu\text{m}$) arranged in a cubic array. The maximum distance between the pillars (pore size) was $= 180 \,\mu\text{m}$ and the minimum (throat) was $t = 40 \,\mu\text{m}$. These geometrical properties yielded in a porosity of 0.39. A similar network pattern was used by Zhang et al. (2011). A cover sheet of Pyrex glass was bonded to the micromodel to seal the channel. The channel was placed horizontally and fluid flow was driven by a pressure gradient imposed with a syringe pump (Harvard apparatus, model PHD 2000) connected to the inlet channel. The outlet was open to atmosphere. The volumetric flow rate was set through the pump controller while the pressure gradient for a single-phase flow was estimated using the relationships reported by Tamayol et al. (2012).

Two immiscible working fluids were used: (*Fluid A*) the wetting phase was obtained by mixing glycerol (G33-500 from Fisher Scientific) and water in a 57% and 43% proportion, respectively, by volume; (*Fluid B*) silicone oil (1378364, from Sigma Aldrich) was used as the nonwetting phase. This choice of this fluid combination was dictated by optical requirements as explained below. The interfacial tension was $\sigma = 11.7$ mN/m, the viscosity ratio was $\mu_A/\mu_B \approx 0.25$ and the density ratio was $\rho_A/\rho_B \approx 1.2$. Due to the limited vertical depth of the microchannel and the horizontal nature of the displacement process, buoyancy effects were negligible in these experiments.

The fluid flow through the 2D porous domain was imaged with a dual-camera μPIV setup with two, 12-bit frame-straddle CCD cameras (TSI 11MP), connected to a microscope (Olympus BX60). A high-energy $10\times$ magnification lens (N.A. = 0.3) was used for imaging and volume illumination was provided by an Nd:YAG, double-pulsed green (532 nm) laser. Fluorescent particles (1 μ m diameter) were added to the flow to track the fluid motion. The characteristics of the particles are provided below based on the fluid phase. The seeding concentration was maintained at approximately 0.04% by volume. For each camera, image pairs were collected at 2 Hz (the maximum frame rate for the system) and an appropriate time interval between laser pulses was chosen in order to optimize the results of image interrogation through correlation.

When imaging a two-fluid system, several optical challenges must be addressed, including refractive index matching (RIM) of the two fluids (Kim et al., 2004) and signal separation (Natrajan and Christensen, 2009; Oishi et al.,

2011). In particular, μ PIV techniques that utilize volume illumination rely on the depth of focus of the imaging system to determine the measurement plane. If the two fluids that are imaged simultaneously by the same camera have different RI, the light rays will follow different paths and result in a discontinuity in the planes imaged. This effect was easily demonstrated using a special microdevice comprised of two parallel channels separated by a thin wall. Figure 2 shows a microscope image of such a two-channel device in which silicone oil (RI = 1.403) is introduced in the top channel and pure glycerol (RI = 1.44) in the bottom channel. Both channels are imaged in the FOV and the effects of RI mismatch are easily observed. To emphasize these effects, a microscopic scale was placed underneath the microdevice, straddling the separating wall. The picture in Fig. 2a is taken focusing the image on the top part of the scale and shows that the bottom part is blurred due to RI mismatch. The fluid combination used here allowed us to correct this effect by accurately matching the RI of the silicone oil (RI = 1.403) with the RI of glycerol by adding water to the glycerol and fine-tuning the concentration ratio. This RIM eliminated the depth discontinuity between the focal planes in the two fluid phases, thus permitting simultaneous imaging of the same plane within the two phases as shown in Fig. 2b.

The second challenge refers to the need to localize the two immiscible fluids in order to associate each velocity measurement to the correct fluid phase. The use of the same tracer particles for both fluids would render the identification of the fluids and the recognition of the interface impossible. To overcome this challenge, the two fluids were seeded with two different fluorescently-tagged tracer particles (1.0 μm). The same coherent light (532 nm) was absorbed by the particles and emitted at two higher but different wavelengths defined by their respective Stokes shifts. More specifically, FluoSpheres® Carboxylate-Modified Microspheres (580/605 nm), provided by Life Technologies Corporation, were dispersed in the aqueous glycerol, while specially manufactured lipophilic Silica microspheres (540/575 nm), provided by Discovery Scientific Inc, were easily dispersed in silicone oil. In order to separate the spectral signals from the fluids, specific dichroic mirrors were placed along the light paths to the cameras allowing the selective collection of the light emitted by the two phases (Fig. 3). The emission from the particles passed through a filter cube that conveyed part of the light (high-pass filter $\lambda > 600$ nm) to Camera α while reflecting the remaining light energy ($\lambda < 600$ nm) to Camera β . Additional filters were used just upstream of the two PIV cameras in order to optimize the signal separation. A high-pass filter ($\lambda > 610$ nm) ensured that only the fluoresced light from particles in Fluid A was imaged by the Camera α , while a band-pass filter (570 ± 10 nm) was used in front of Camera β to selectively collect the light emitted only by particles in Fluid B. An example of particle images collected in the test channel is reported in Fig. 4. Although the signal separation is not perfect, the images show that the cross-talk between the two spectra is minimized. Additionally, the light intensities from the two tracers were very different. Figure 4a shows that the particles dispersed in the aqueous glycerol have a stronger signal than those dispersed in silicone oil. This difference was quantified for each camera by calculating the mean intensity distribution of the two tracers and this information was utilized to inform a masking function that assisted in the automatic identification and tracking of each

MicroPIV images were acquired far from the inlet of the microchannel (in the second half) to minimize preferential paths that may be generated by inlet effects. The use of a $10\times$ objective provided a 2 mm diameter imaging area allowing the observation of approximately four pore spaces across the diameter at high spatial resolution ($\approx 0.65 \, \mu \text{m/pixel}$). The flow was kept constant during each experiment at two different flow rates, 0.5 and 1 ml/min, resulting in flow velocities up to 0.2 ms⁻¹. The system allowed sequences of consecutive images to be captured with a maximum of 200 image pairs. Due to this storage limit, the image acquisition was started only when the interface approached the measurement region in order to focus the measurements on interface processes. The maximum time duration of each experiment was 100 seconds. This time was found to be long enough to characterize steady-state single-phase flow while, for fluid-fluid interaction, we found that longer acquisition time coupled with faster frame rate would be beneficial for a more in-depth investigation of these phenomena.

An iterative cross-correlation interrogation procedure employing local window offsets defined by the local bulk fluid motion was utilized to maximize spatial resolution and significantly reduce PIV uncertainties associated with loss of particle pairs. An interrogation window of 16×16 pixels with 50% window overlap was used, thus allowing us to resolve instantaneous flow fields at high spatial resolution (i.e. 5 μ m grid spacing).

RESULTS

Experiments were conducted in two stages: both imbibition (wetting displacing the nonwetting phase) and drainage (nonwetting displacing the wetting phase) cases were considered. The first stage involved saturating the micro-device with one of the two fluids (*resident* fluid) and the goal was to quantify the flow once steady-state conditions were achieved. The second stage involved ceasing injection of the resident fluid and beginning the injection of the second phase (*displacing* fluid) into the fluid-saturated device in order to observe fluid-fluid front migration. For this second category of experiments, particular care was given to avoid intrusion of air into the conduit in order to obtain a clean interface between the two liquids.

Single-Phase Flow

Although single-phase flow was not the focus of this study, measurements under these conditions were taken to establish a quantitative basis of comparison with the more complex two-phase flow conditions. The images were captured with a single camera setup but with the same optical configuration that was then used for two-phase experiments. These initial measurements were also useful to assess the performance of the acquisition parameters and to optimize the image quality (e.g. seeding concentration, laser energy). Additionally, these preliminary data provided valuable information for identifying and tracking the interface in the two-phase experiments. In particular, images collected in these experiments allowed us to test, for each working fluid, particle response in terms of light intensity and thus calibrate automatic mask processing schemes.

Figure 5 shows an example of a particle image obtained by injecting aqueous glycerol at a constant rate (1 ml/min) into the porous micromodel. The circular dark regions are associated with the solid micro-pillars, while flowing fluid is observable due to a uniform distribution of tracer particles. Figure 6 shows the velocity distribution obtained by ensemble averaging 200 instantaneous flow fields under these conditions. The flow shows a very periodic pattern that extends over the entire field of view (Fig. 6a), which is consistent with the regular geometry of the porous network. As expected, since the flow is in the laminar regime ($Re \sim 10^1$), symmetrical patterns with respect to each solid element are observed. These high-resolution velocity fields allowed analysis at the pore-space scale (see Fig. 6b) to identify the features that characterize pore flow. Flow alternates between converging towards the pore space and splitting into the troughs. Flow at the inlet and outlet are symmetrical and stagnation points are observed at the front and back of each pillar in a symmetric fashion. Particles follow pseudo-sinusoidal paths undergoing periodic deceleration/acceleration cycles as they move from trough (maximum velocity) to pore body (minimum velocity) and vice-versa, respectively. As expected for laminar flow, these accelerations occur in the absence of any observable flow separation or local instability. Vorticity fields (not reported here) show intense shear at the fluid-solid interface with increasing shear at the trough owing to viscous stresses. Similar single-phase flow experiments were conducted injecting silicone oil as the working fluid and identical flow patterns were observed, as expected.

Two-Phase Flow

After saturation of the microchannel with a single phase and collection of steady-state flow measurements, the injection of the first working fluid was stopped. The second stage of the experiments involved beginning injection of the second working fluid and, without introducing perturbation in the system, preparing the two-camera setup to capture the fluid-fluid interaction. Both imbibition and drainage cases were measured and here we report an example of each case and discuss the most significant mechanisms observed.

Figure 7 presents an example of fluid-fluid interaction for the case of drainage showing the displacement of the wetting phase (aqueous glycerol, Fig. 7a) induced by the penetration of the nonwetting phase (silicone oil, Fig. 7b). These snapshots show the penetration of silicone oil is imaged in the field of view and thus flow in both fluid phases is simultaneously quantified. The results show that the flow organization typical of the single-phase case is dramatically destroyed. In neither of the two phases in Fig. 7 does the flow follow sinusoidal paths. Instead, the flow tends to channel along preferential and irregular flow paths of high and low momentum. In the specific pore network used here, these flow paths tend to be straight over multiple pore necks (typically two or three) and follow the diagonal (45°) direction. The flow direction occasionally (i.e. without a clear periodicity) switches by a 90° angle, facilitating migration of the interface downstream.

Several interface migration mechanisms were observed in our experiments, reflecting some of the mechanisms that Lenormand and Zarcone (1988) observed in porous networks with different structures. In Fig. 8 we report a specific case in which a quasi-straight interface was observed during its migration. The interface was oriented at an approximately 45° angle and appeared to maintain its configuration as it moved downstream for the entire observation period (3 sec). Here we focus the discussion on the flow induced by the interface as it advects across the field of view rather than on the dynamics of the interface (Fig. 8). To our knowledge, the results reported herein represent the first attempt to quantify the flow near a fluid-fluid interface moving through a porous network. Six steps of this unsteady phenomenon were observed. The first snapshot (Fig. 8a) shows the velocity distribution when the interface is located at the extreme right of the field of view and is migrating to the left. Despite the fact that the porous domain downstream of the interface is still saturated with a single phase (aqueous glycerol), the results reveal that several fundamental differences exist between this case and steady-state, single-phase flow (Fig. 6). For example, Fig. 8a shows that the high-momentum regions are not necessarily located at the troughs. We observe that some pore spaces exhibit flow velocity magnitudes higher than neighboring pore necks. As the interface approaches (Fig. 8b,c), the flow distribution remains rather similar with high flow irregularities. These results reveal that the primary effect of an approaching interface (Figs 8a-c) is the perturbation of the pattern that had been previously established in the steady-state, singlephase flow, with regions of high and low momentum irregularly distributed across the flow domain. observations suggest that the flow is driven by local pressure gradients that continuously change intensity and direction rather than by a macroscopic pressure gradient as previously proposed by Berg et al. (2013). This behavior also suggests that the flow instabilities (i.e. Haines jumps) due to interface migration may induce pressure instabilities that propagate further downstream, thus perturbing the wetting phase. The fluid "senses" that the interface is approaching and the structure of the flow (typical of a steady-state, single-phase flow condition) is perturbed before the actual passage of the interface. Additionally, the flow sequence reported in Fig. 8 highlights that this scenario of instability persists during the entire passage of the interface. This phenomenon leads to separation of aqueous glycerol droplets that remain trapped within the pore space. Classic models (Lenormand and Zarcone, 1988) suggest that the mechanisms that control such trapping are governed by viscous and capillary forces. However, recent studies suggest that inertial forces associated with Haines jumps may play a critical role. The linkage between the flow distribution and the formation of residual pockets is currently under investigation as the quantitative technique presented herein could shed significant light on these fundamental processes.

The second case of two-phase flow dynamics captured concerns the flow distribution in the pore network after the passage of the interface. For this condition we discuss the case on imbibition (aqueous glycerol penetrating a domain saturated with silicone oil) and focus on one particular snapshot (see Fig. 9) that illustrates the flow behavior immediately after the passage of the interface (~ 0.5 sec). In Fig. 9, the flow field is superimposed on the raw particle image to maximize the information that can be extracted from a single realization. First, the velocity vectors are not visible everywhere, although interrogation was performed over the entire field of view. This means that certain regions where particle images exist are devoid of fluid motion. In addition to the dark circular regions that correspond to the porous matrix, there exist dark areas connecting the pillars. These latter dark regions correspond to trapped pockets of silicone oil. Additional dark regions surrounded by a sharp bright boundary are visible in Fig. 9 and represent air bubbles that were unintentionally introduced in the flow and transported by the liquid-liquid interface. They remain trapped due to strong capillary forces. Their shape reveals the local pressure gradient and provides insight as to the elastic energy that can be accumulated in pore spaces and troughs. Finally, static pockets of aqueous glycerol are highlighted in Fig. 9 by regions in which tracer particle images are evident but velocity is found to be zero. These regions of stagnant flow appear to be randomly distributed and they affect the neighboring pore flow processes by altering the local pore connectivity and thus the global permeability. In short, Fig. 9 illustrates the coexistence of several regions, each of which are characterized by different fluids and/or kinematic states. This situation results in complex and irregular patterns of preferential flow paths (where vectors are visible) that are referred to as *channeling*. These flow channels are characterized by a number of flow features such as confluences, bifurcations and stagnation regions. In such channels, the flow undergoes acceleration and occasional changes of direction that can occur over very short timescales ($\sim 10^{-3}$ sec).

These measurements reveal that the flow patterns established after the passage of the interface are highly dynamic and that the preferential paths continue to change, with flow abruptly switching direction and magnitude but maintaining a channeling-type of flow organization (i.e., flow is limited to certain pore spaces). In addition, it was observed that the number of independent flow channels can vary in time. Bifurcations tend to distribute the flow over a larger area with lower shear stresses while confluences tend to concentrate flow into fewer channels characterized by a higher flow rate and thus higher shear stresses. These two competing mechanisms govern the distribution of flow in the network and reflect the energy balance between viscous dissipation and elastic energy accumulated via capillary forces. Our experiments indicate that the flow does not tend towards the lower energy dissipation configuration (i.e., higher number of channels) immediately after the passage of the interface. Unfortunately, the limited duration of data acquisition did not allow identification of a clear trend.

To our knowledge, the patterns described herein have not been observed before. Previous studies in similar pore networks have in fact focused their attention on the interfacial processes, but using qualitative approaches. Classic studies were focused on tracking the evolution of the interface over a larger length scale and hence neglected the tail of the fluid-fluid transition as flow in such regions could not be resolved. Recently, experimental insight into this dynamic behavior was provided by pressure measurements conducted by Moebius et al. (2012) under both drainage and imbibition scenarios. The present measurements indicate that investigating the flow processes induced by the passage of the interface is very important for understanding phenomena such as capillary trapping and pressure fluctuations due to elastic energy dissipation.

CONCLUSIONS

In this work, an experimental technique to quantify two-phase flow processes in 2D permeable media was presented. This flow configuration underlies a range of applications across engineering and science, including contamination of groundwater reservoirs, enhanced oil and gas recovery and geological carbon sequestration. The ability of the technique to capture peculiar details of the flow was demonstrated and some unique preliminary data were reported showing, for the first time, the flow distribution of phenomena that had been previously observed only qualitatively (i.e., front migration). These results highlight a particular step of penetration of the silicone oil phase into the initial wetting fluid (aqueous glycerol). Long sequences of velocity data reveal subsequent steps of this process showing the penetration of silicone oil through preferential fluid paths. Sequential images show that the flow is highly unstable, with abrupt changes of velocity and direction which suggest the onset of energetic bursts termed Haines jumps. However, due to the extremely short time scales of these events, time-resolved quantification of these events was not possible. A detailed quantification of the flow during these events will require use of high-speed image acquisition.

Other distinctive fluid patterns, such as pools, thin films, bridges and cones qualitatively observed in previous work, are presently under investigation herein in a quantitative fashion. This will allow quantification of fluid-dynamic interfacial processes that control short time-scale trapping mechanisms (i.e. hydrodynamic and capillary trapping) which might have impact on longer time-scale geochemical reactions (e.g. dissolution and precipitation of minerals).

ACKNOWLEDGEMENTS

The authors gratefully acknowledge the support of the International Institute for Carbon Neutral Energy Research (WPI-I2CNER), sponsored by the World Premier International Research Center Initiative (WPI), MEXT, Japan. The first author (G. B.) also gratefully acknowledges funding from the Ross Jackson Postdoctoral Fellowship at the University of Illinois.

REFERENCES

- [1] Bandara UC, Tartakovsky AM and Palmer BJ (2011) Pore-scale study of capillary trapping mechanism during CO₂ injection in geological formations, International Journal of Greenhouse Gas Control, doi:10.1016/j.ijggc.2011.08.014.
- [2] Berg, S., Ott, H., Klapp, S. A., Schwing, A., Neiteler, R., Brussee, N., ... & Stampanoni, M. (2013). Real-time 3D imaging of Haines jumps in porous media flow. Proceedings of the National Academy of Sciences, 110(10), 3755-3759.
- [3] Crawford, F. W., & Hoover, G. M. (1966). Flow of fluids through porous mediums. Journal of Geophysical Research, 71(12), 2911-2917.
- [4] Haines, W. B. (1930). Studies in the physical properties of soil. V. The hysteresis effect in capillary properties, and the modes of moisture distribution associated therewith. The Journal of Agricultural Science, 20(01), 97-116.
- [5] Jerauld, G. R. and Salter, S. J. (1990) The Effect of Pore-Structure on Hysteresis in Relative Permeability and Capillary Pressure: Pore-Level Modeling. Transport in Porous Media. 5: 103-151.
- [6] Kim BJ, Liu YZ and Sung HJ (2004) "Micro PIV measurement of two-fluid flow with different refractive indices" Meas. Sci. Technol. 15: 1097–1103
- [7] Krummel, A. T., Datta, S. S., Münster, S., & Weitz, D. A. (2013). Visualizing multiphase flow and trapped fluid configurations in a model three-dimensional porous medium. AIChE Journal. 59(3) 1022-1029. doi 10.1002/aic.14005.
- [8] Lenormand R, Touboul E and Zarcone C (1988), Numerical models and experiments on immiscible displacements in porous media, J. Fluid Mech, 189, 165-187.
- [9] Lenormand R, Zarcone C and Sarr A (1983), Mechanisms of the displacement of one fluid by another in a network of capillary ducts, J. Fluid Mech, 135, 337-353.
- [10]MacMinn C, Szulczewski M, Juanes R (2010) CO₂ migration in saline aquifers. Part 1. Capillary trapping under slope and groundwater flow. J. Fluid Mech. 1–23.
- [11]Meakin P & Tartakovsky AM, (2009). Modeling and simulation of pore scale multiphase fluid flow and reactive transport in fractured and porous media. Rev. Geophys. 47, RG3002.
- [12] Moebius, F., & Or, D. (2012). Interfacial jumps and pressure bursts during fluid displacement in interacting irregular capillaries. Journal of colloid and interface science.
- [13] Moebius, F., Canone, D., & Or, D. (2012). Characteristics of acoustic emissions induced by fluid front displacement in porous media. Water Resources Research, 48(11).
- [14] Natrajan, V. K., & Christensen, K. T. (2009). Two-color laser-induced fluorescent thermometry for microfluidic systems. Measurement Science and Technology, 20(1), 015401.
- [15]Oishi, M., Kinoshita, H., Fujii, T., & Oshima, M. (2011). Simultaneous measurement of internal and surrounding flows of a moving droplet using multicolour confocal micro-particle image velocimetry (micro-PIV). Measurement Science and Technology, 22(10), 105401.
- [16] Tamayol, A., Khosla, A., Gray, B. L., & Bahrami, M. (2012). Creeping flow through ordered arrays of micro-cylinders embedded in a rectangular minichannel. International Journal of Heat and Mass Transfer.
- [17] Yuan, H. H., & Swanson, B. F. (1989). Resolving pore-space characteristics by rate-controlled porosimetry. SPE Formation Evaluation, 4(1), 17-24.
- [18]Zhang C, Oostrom M, Wietsma TW, Grate JW and Warner MG (2011) Influence of viscous and capillary forces on immiscible fluid displacement: pore-scale experimental study in a water-wet micromodel demonstrating viscous and capillary fingering. Energy Fuels. 3493-3505.

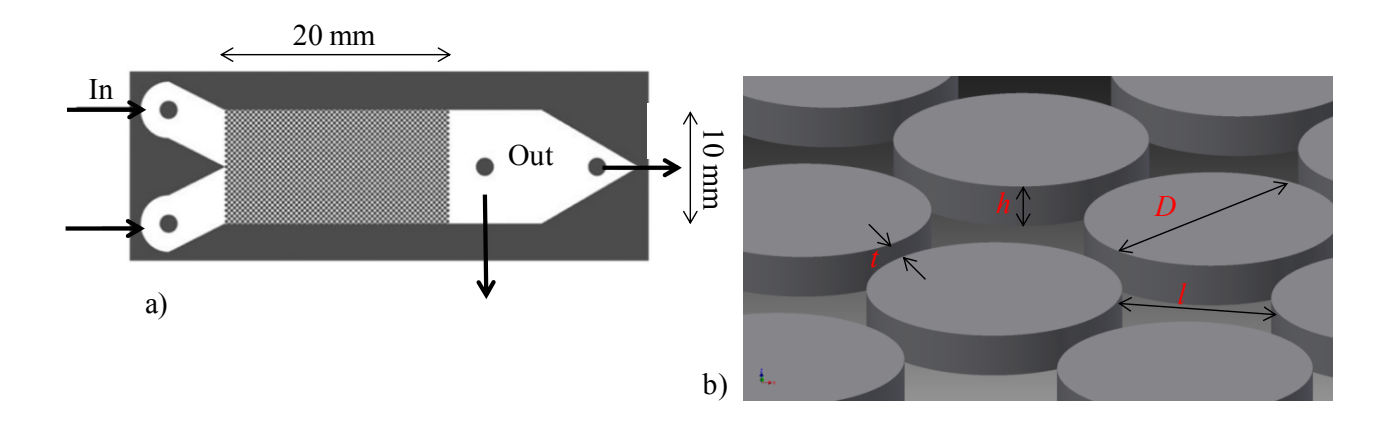


Figure 1. Schematic of the porous microchannel geometry. a) Top view; b) Perspective view.

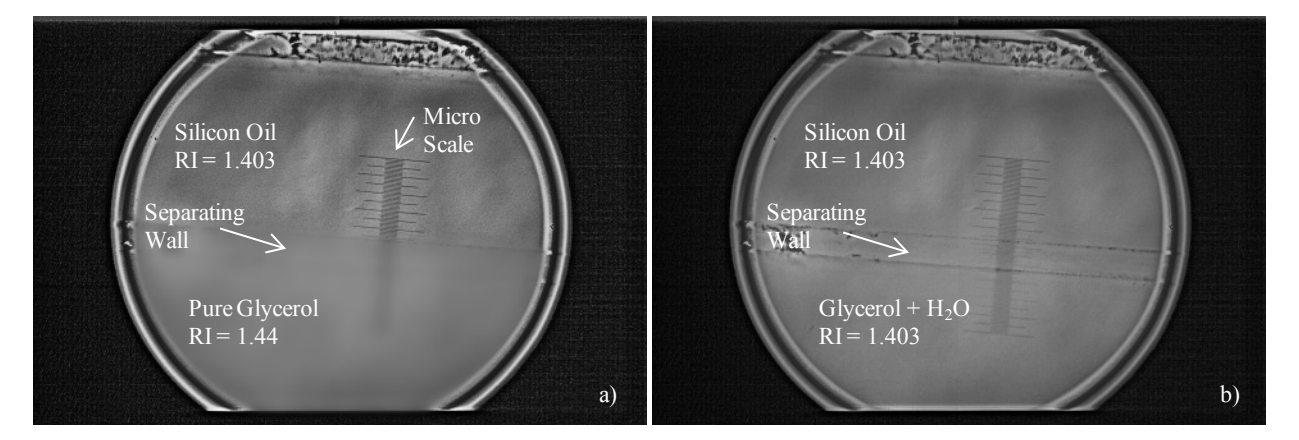


Figure 2. Visualization of a microscopic calibration scale immersed in a microchannel containing two different fluids separated by a wall (indicated in the figure). In both cases, the same silicone oil is used. a) Pure glycerol; b) Aqueous glycerol: 57% glycerol and 47% water.

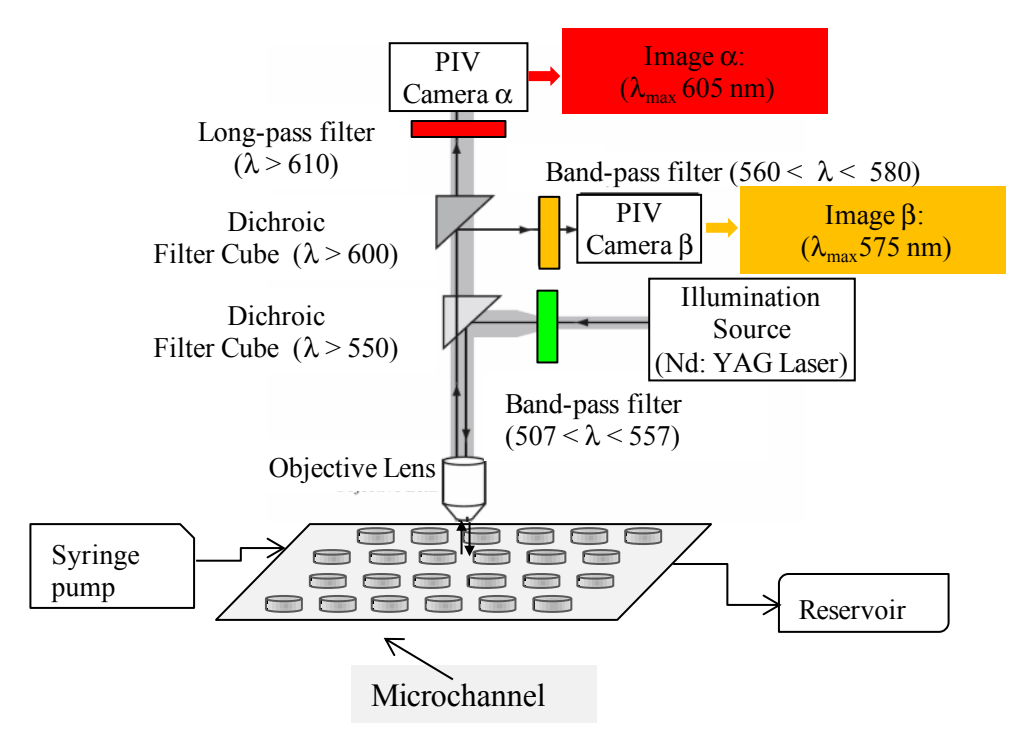


Figure 3 Dual-camera μPIV setup illustrating the optical separation methodology employed.

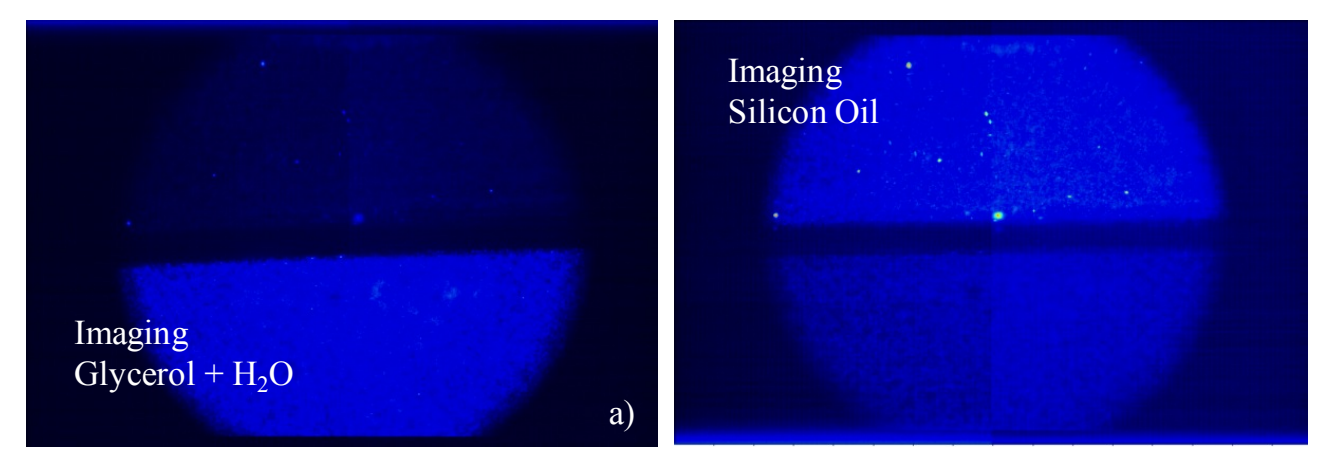


Figure 4. Example of particle images acquired by the two cameras highlighting the efficacy of the signal separation. a) *Camera* α ; b) *Camera* β .

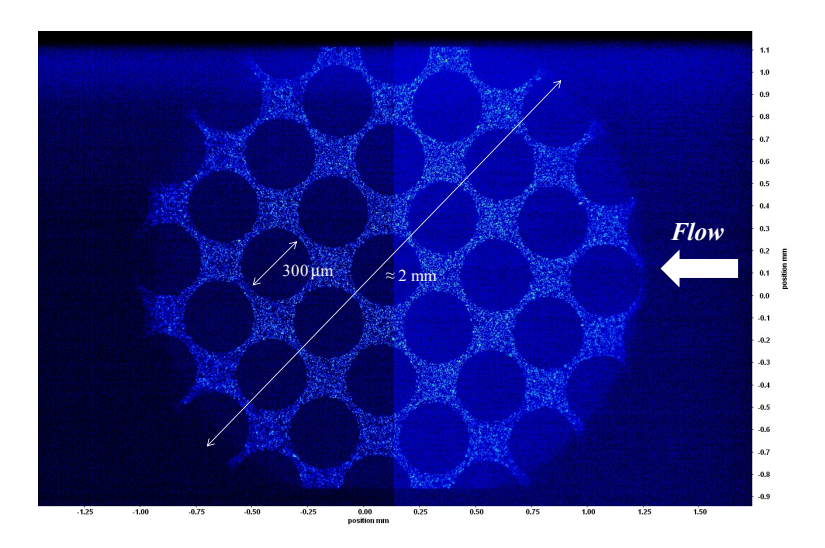


Figure 5. Representative particle image obtained using a μ PIV setup for single-phase flow (aqueous glycerol) infiltrating the 2D permeable micro-device. Flow rate Q = 1 ml/min.

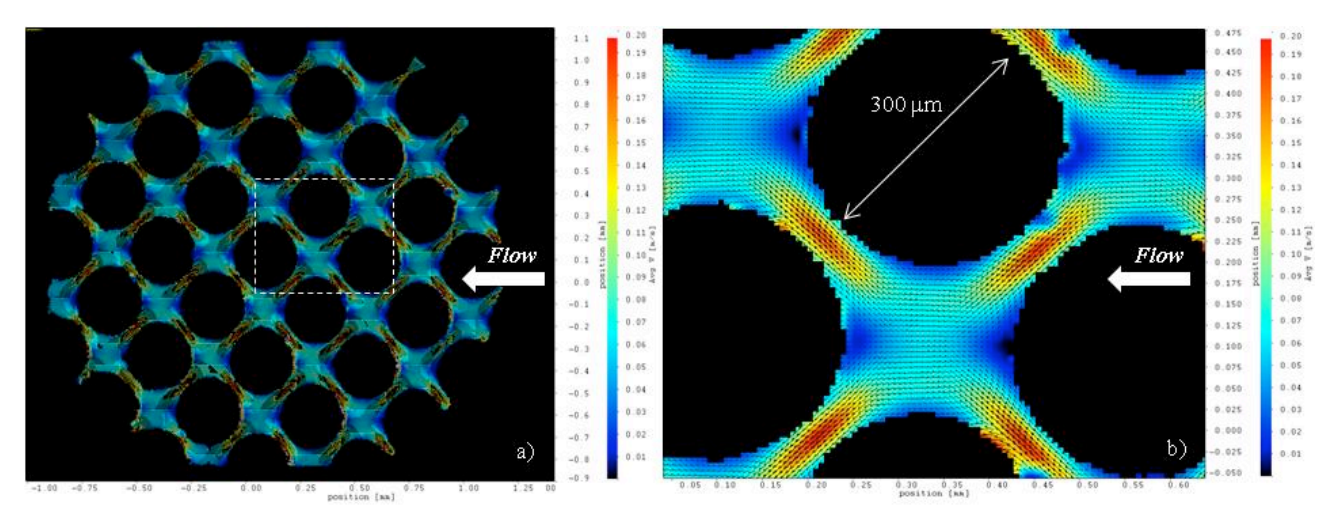


Figure 6. Velocity distribution in of single-phase flow (aqueous glycerol) infiltrating the 2D permeable micro-device under steady-state conditions. a) Entire field of view; b) Zoomed-in view showing vector field at the pore-space scale (Contours show velocity magnitude). Flow rate Q = 1 ml/min.

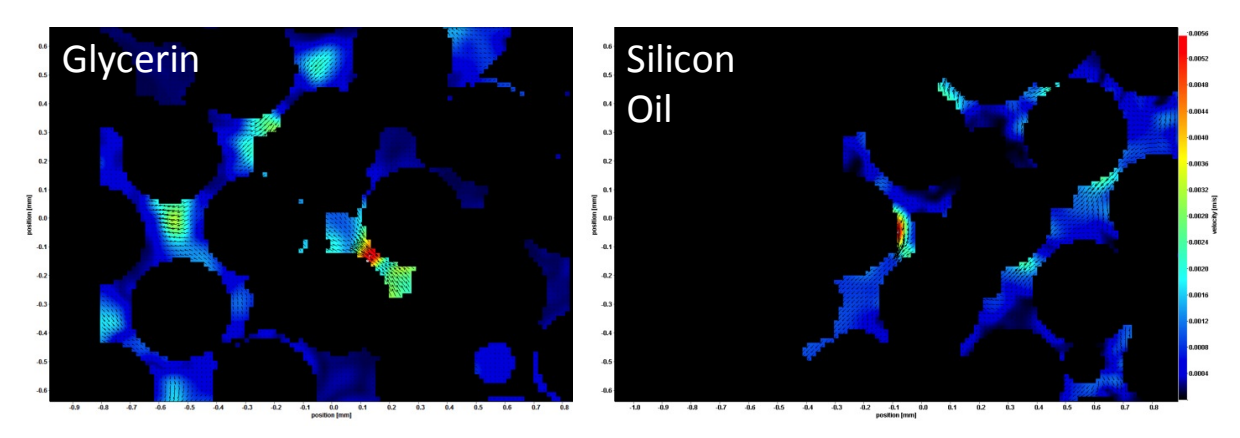


Figure 7. Velocity distribution at the interface of two-phase flow during a drainage experiment (penetration of silicone oil into aqueous glycerol). Images show displacement of: (a) aqueous glycerol and (b) silicone oil. (Contours represent velocity magnitude).

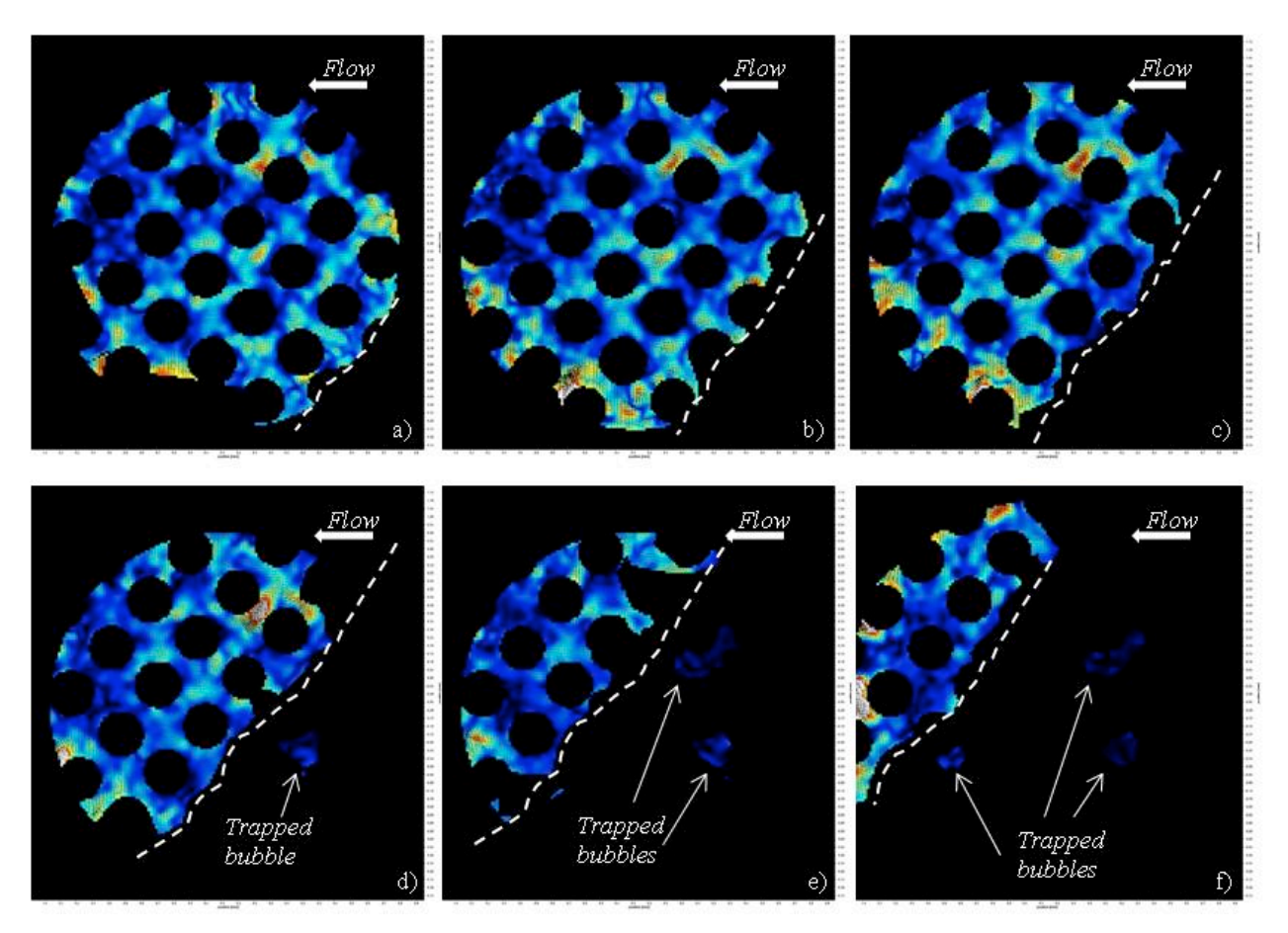


Figure 8. Velocity distribution in the aqueous glycerol showing six evolution steps of the interface (dashed line) migration and bubble trapping dynamics. (Contours show velocity magnitude).

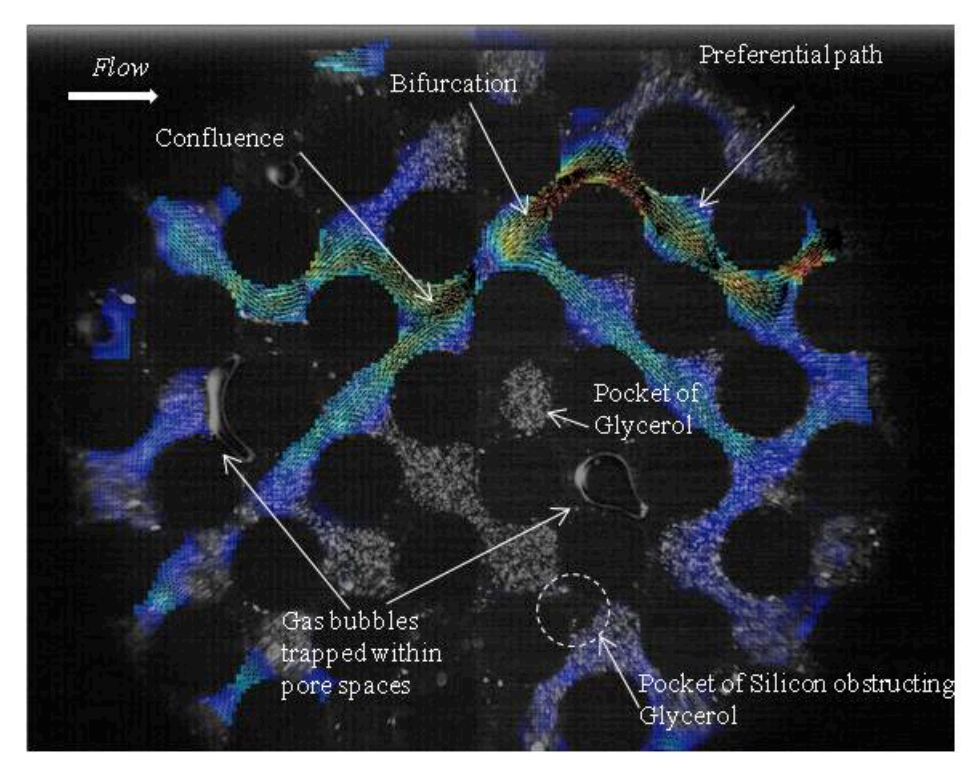


Figure 9. Velocity distribution of aqueous glycerol penetrating silicone oil after passage of the interface. The image shows an example of a preferential flow path (Contours show velocity magnitude).